Chapter 2

Experimental methods

In this chapter we will describe the details of the experimental setups and the techniques specifically developed for analyzing the samples.

2.1 Raman spectroscopy

Light can interact with matter in various ways: it can be reflected, absorbed, transmitted and scattered. We can make a further distinction of scattering processes, classifying them into two types: elastic scattering, when the energy (wavelength or frequency) of photons is preserved, or inelastic, when it changes during the process. Among the various inelastic scattering processes we find Raman scattering, a type of inelastic process that was predicted by Smekal in 1923 and experimentally observed for the first time by Raman and Krishnan in 1928 [266–269].

In order to understand the physical process behind Raman scattering it is necessary to consider the quantized energetic levels that characterize the sample under examination (e.g. a molecule or a crystal). The vibrational energetic structure of materials ischaracterized by a fundamental electronic

57

level and a series of vibrational levels located at energies higher than the ground state. At $0\,\mathrm{K}$ only the fundamental level is populated, since there is not sufficient energy to excite atomic motions (vibrations) and therefore to populate upper-lying vibrational levels. At temperatures larger than $0\,\mathrm{K}$ the various vibrational modes (characterized by different energies) can be progressively populated, leading to the unlock of atomic or molecular vibrations. The energy difference between adjacent vibrational levels is comparable with the energy of photons in the IR regime, and can be probed either by the so-called Infra-Red Spectroscopy, or with the Raman spectroscopy. The two techniques are complementary, however, one advantage of Raman is that it can employ light in the visible range, much easier to handle and to detect.

When an incident visible photon impinges on the sample, it can promote the transition of the system to a formerly unoccupied state, called *virtual state*. The name *virtual* does not indicate that this is not a real energetic level, but rather that it is not an energetic level that is allowed by the Hamiltonian of the sample, but that is created after the light-sample interaction. Following this event, the great majority of the impinging photons undergoes an elastic scattering process: after they are absorbed by the sample, causing the transition from the initial state to the virtual states, they are re-emitted with the same energy (Figure 2.1 b).

It may however happen that, when emitting a photon, the system does not decay back to the original starting state. In this case, the emitted photon energy differs with respect to the excitation energy. If the energy of the scattered photon is lower than the energy of the incident beam, the process is called Raman Stokes process (Figure 2.1 a); on the other hand, if the system is initially found in an excited energetic level, and decays to a state with lower energy, than the energy of the scattered photon is higher than the en-

ergy of the impinging one; this process is instead called anti-Stokes Raman scattering (Figure 2.1 c) [270].
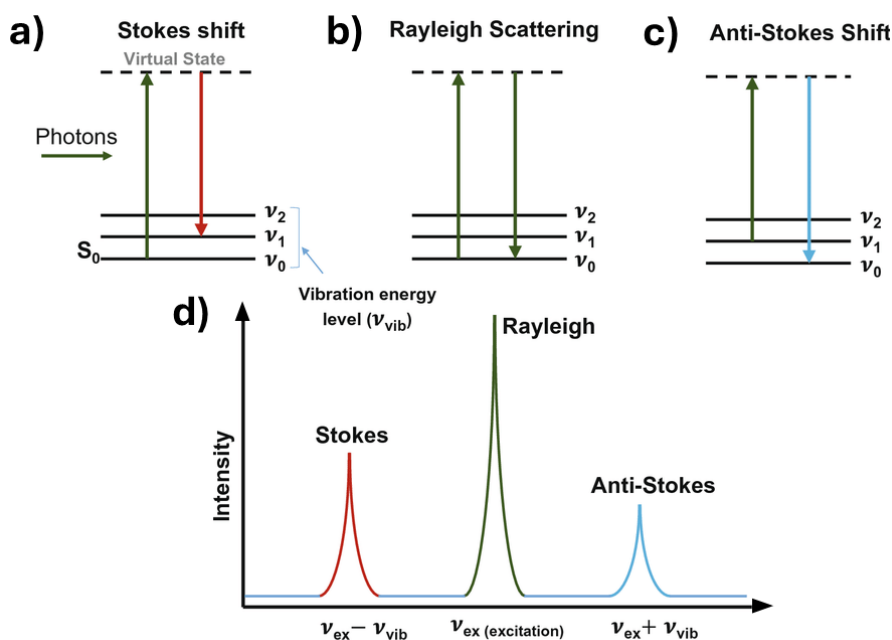

Figure 2.1: a) Sketch of the Stokes Raman scattering process. b) Sketch of the elastic (Rayleigh) scattering process. c) Sketch of the anti-Stokes Raman scattering process. d) Schematic representation of a Raman scattering spectrum where the elastic and the inelastic peaks are highlighted. Adapted with permission from Ref. [271] Copyright 2020 Springer Nature.

Since (in the absorption or in the emission process) the vibrational states of the sample are actively involved in the Raman scattering, probing the scattered photons can yield useful information about the vibrational (hence structural) properties of the investigated sample.

In this respect, it is important to notice that not all vibrational modes can take part in Raman processes because Raman scattering takes place only between vibrational modes that involve a variation in the polarizability of

59

the sample. For centrosymmetric molecules the modes that are active for IR light absorption are Raman-inactive and vice versa so that for these systems Raman is a complementary technique on respect to IR spectroscopy [272].

Since very few photons (typically 1 out of 10^6 or 10^8) undergo a Raman scattering process, Raman peaks are characterized by reduced intensity with respect to the incident beam (Figure 2.1 d) and thus surface enhances spectroscopies, that uniquely enable the amplification of thiny optical signals, assume a key role [273–276].

As anticipated in section 1.1.2, the ratio between the anti-Stokes and the Stokes intensity peaks can be exploited as a temperature measurement, since the population of the vibrational states (the starting points for the anti-Stokes process) is determined by the system's temperature according to the Boltzmann distribution [75].

The instrument we used for this thesis work is a Jasco NRS-4100® confocal Raman microscope described in detail in other works [277].

2.2 (Imaging) Photoluminescence spectroscopy

Photoluminesce (PL) is the process involving the emission of photons from a material after is has been irradiated with photons of different (larger) energy (Figure 2.2 a), it is common in certain classes of semiconductors or insulators, while it is essentially absent in metals. We will focus on the phenomen of PL in semiconductors, where the process is strictly related to the presence of an electronic band gap in the electronic structure, separating occupied and unoccupied states.

When a semiconductor is irradiated with photons with an energy higher (or

equal) than the band gap, electrons from the occupied valence band can be promoted to the unoccupied conduction band, absorbing the energy of the impinging light. Electrons in the conduction band may relax back into the valence band through the emission of energy in the form of photons (Figure 2.2 b).

An electron ecited in the conduction band typically relaxes towards the band bottom via non-radiative processes on a time scale much faster than the time scale for the radiative relaxation to the valence band. Analogously, the holes in the valence band relax towards the top of the band in short times. This means that the photons emitted following the radiative decay of electrons from the conduction to the valence band will typically have an energy very close to the value of the energy gap of the material.

In materials characterized by a strong excitonic behaviour (like 2D TMDC) the main emission channel occurs through the recombination of excitons because the excitonic band gap is the real optical gap these materials (the smallest energy difference between occupied and unoccupied levels).

The instrument we employed to characterize the spatial dependence of the PL of the analyzed systems is the Jasco NRS-4100® confocal Raman microscope (Figure 2.2 c). The instrument enables the acquisiton of hyperspectral-maps with micrometric resolution, where at each pixel of the map is associated a PL spectrum.
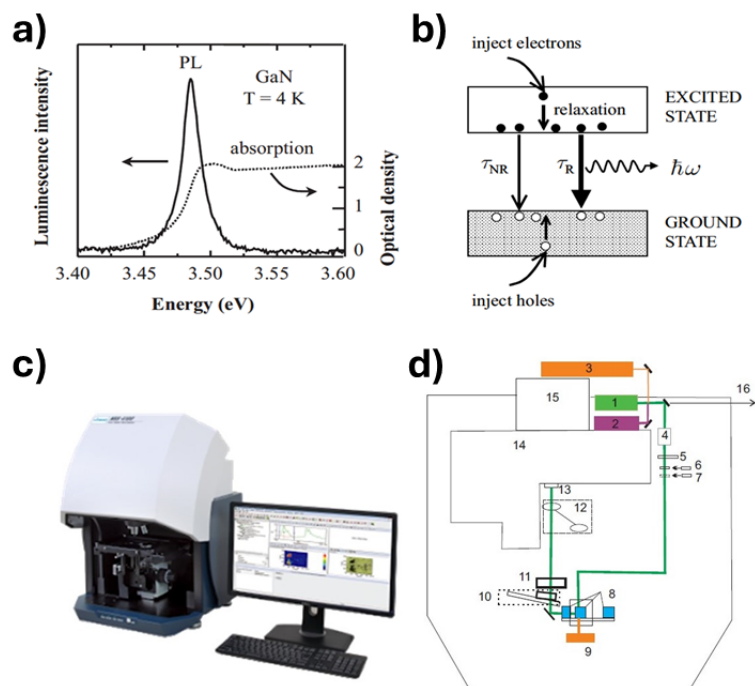
61

Figure 2.2: a) PL and absorption spectra of gallium nitride (GaN) at 4 K. It is apparent that the seminconductor can absorb photons with energies larger than the band gap, but mainly emits photons at energies slightly lower than the band gap. b) Schematics of the PL process after the excitation of electrons in the conduction band. c) Picture of the Jasco NRS-4100® confocal Raman microscope. d) Scheme of the main components of the Jasco NRS-4100® confocal Raman microscope. Panel a) and b) reprinted with permission from Ref. [90] Copyright 2002 Oxford University Press. Panel c) and d) adapted with permission from Ref. [277].

2.3 (Imaging) Spectroscopic ellipsometry

2.3.1 Spectroscopic ellipsometry

Spectroscopic ellipsometry (SE) is one of the most complete characterization techniques for the investigation of the optical response of materials. It is based on the analysis of the variation of the state of polarization of light after reflection from a given sample (Figure 2.3 a).

Such a variation is expressed in terms of two quantities, Ψ and Δ, related to the complex p-polarized and s-polarized Fresnel coefficients of the samples (labelled r_p and r_s respectively) through the relation 3.1, called *fundamental equation of spectroscopic ellipsometry* [92, 96]:

$$\rho = \frac{r_p}{r_s} = \frac{\left(\frac{E_{rp}}{E_{ip}}\right)}{\left(\frac{E_{rs}}{E_{is}}\right)} = tan\Psi \cdot e^{i\Delta}. \tag{2.1}$$

From the experimental determination of $\Psi(\lambda)$ and $\Delta(\lambda)$ it is possible to retrieve both optical and morphological information about the sample under scrutiny, via the application and refinement of appropriate optical models. For example it is possible to obtain the dielectric function of the investigated material and/or the layer thickness in stratified samples. The dielectric function describes in a complete way the optical response of a given material following the interaction with light.

In the present thesis, we have employed two spectroscopic ellipsometers, i.e. instruments that perform measurements of the Ψ and Δ quantities as a function of the light wavelenght λ. The first one is a J.A. Woollam M2000 ® rotating compensator ellipsometer which operates in the wavelength range (245-1670) nm (Figure 2.4 a), while the second is a J.A. Woollam VASE ® which operates in the wavelength range (190-1700) nm (Figure 2.4 b).

2.3.2   Imaging spectroscopic ellipsometry

Traditional SE employs a spot size in the order of mm^2 or cm^2 and is therefore best suited for samples that are spatially homogeneous in these ranges. However, many appealing systems, like 2D materials, are characterized by spatial inhomogeneities on length scales of just a few μm. These materials have to be analyzed with great care in order to fabricate micro and nanodevices. In order to fullfill these recent necessities, a new type of SE was

developed, called Imaging Spectroscopic Ellipsometry (iSE).

This technique couples the SE characterization with the microscopic resolution, enabling the realization of hyperspectral imaging. $\Psi(\lambda)$ and $\Delta(\lambda)$ maps of the sample can be obtained with a spatial resolution of the order of few μm; then, applying a suitable optical model to reproduce the Ψ and Δ values, it becomes possible to determine the dielectric function and the thickness of a given sample with micrometric resolution.

The instrument that was employed in the present thesis is a nanofilm_ep4 from Accurion GmbH $^{\circledR}$ (Figure 2.4 c), that adopts the Polarizer - Compensator - Objective - Analyzer - Detector configuration as emphasized in Figure 2.3 b).
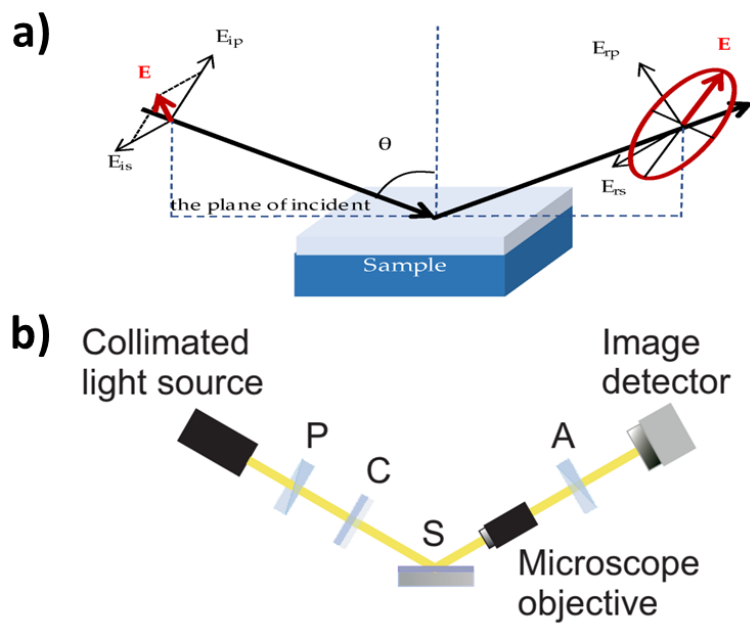
Figure 2.3: a) Schematic of the general working principle of spectroscopic ellipsometry: a light beam with a known intensity and polarization state impinges on the sample, and the polarization state of the reflected beam is characterized. b) Schematics of the iSE setup in the particular configuration of the Accurion GmbH nanofilm_ep4 ®. Before inpinging on the sample the state of polarization of the beam is manipulated by a polarizer and a compensator, after the reflection the imaginng is enabled by an objective and the polarization state is assessedd through another polarizer (analyzer) [96].

Figure 2.4: a) J.A. Woollam M2000 ® rotating compensator ellipsometer. b) J.A. Woollam VASE ® spectroscopic ellipsometer c) Nanofilm_ep4 from Accurion GmbH ®.

2.4 Atomic force microscopy

Atomic Force Microscopy (AFM) is a scanning-probe technique which exploits a nanometric silicon tip to assess the morphology of samples with nanometric resolution. The real probe is the van der Waals interaction between atoms on the tip apex and the atoms of the surface. This interaction is highly dependent upon the distance between the atoms (the tip-sample distance) and quantitatively described by the Lennard-Jones potential [278–281].

In particular, at short distance the interaction is repulsive, due to the Pauli exclusion principle, while at larger tip-sample distances the interaction becomes attractive (Figure 2.5 a). The tip-sample interactions cause a bending of the cantilever where the tip is mounted, which depends from the morphology of the sample. The tip deflection is monitored through the optical lever method. To this end, cantilvers are usually coated with reflective materials; a laser beam is sent impinging on the cantilever and reflected on a photosensor capable of detecting its deflection with a high signal-to-noise ratio (Figure 2.5 b).

AFM can operate in various ways depending on the regime of the interaction between the tip and the sample:

- *Contact mode*: when the tip is kept extremely close to the sample, this modality enables the highest resolution because the repulsive interaction has a more severe dependence upon the atomic distance. One drawback is that in this way it is possible to damage delicate samples like biological ones;

- *Non-contact mode*: when the tip is kept at a certain distance from the sample and the interaction is mainly attractive. This technique is

less invasive, but the spatial resolution of the morphological analysis is highly reduced;

- *Tapping mode* when the tip is kept in oscillation around its resonating frequency and periodically moves from the repulsive to the attractive regime. In the tapping regime it is possible to combine the sensitivity of the contact mode together with the non-invasive approach of the non-contact one. For this reason this is the most adopted mode and also the way used for the characterizations described in this thesis.
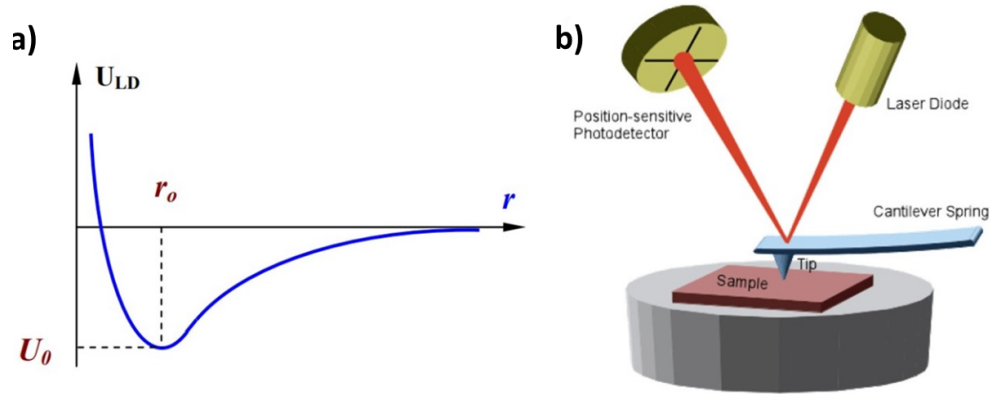

Figure 2.5: a) Schematic of the Lennard-Jones potential where is is possible to identify the repulsive regime (for shorter atomic distances) where decreasing the distance the energy increases and the attractive regime (for longer atomic distances) where increasing the distance the energy increases. b) Schematic of the main components of an AFM setup. Reprinted with permission from Ref. [282].

2.5   Ultrafast transient absorption spectroscopy

Transient absorption spectroscopy (TAS) is a powerful optical pump-probe spectroscopic technique that enables the investigation of transient dynamics in physical systems with temporal resolutions as low as few tens of fs (10^{-15}s).

The experimental setup is drawn in Figure 2.6: an ultrashort electromagnetic pulse, referred to as *pump*, is sent impinging onto the sample causing a perturbation in its electronic structure. In our case the pump wavelength is chosen to be close to the resonant LSPR wavelength, in order to excite the heaters. A second ultrashort pulse (*probe*) is then sent impinging on the system with a delay time τ, that can be experimentally varied. The difference between the optical response of the unperturbed system and the optical response of the system at a time τ after the pump is then measured and recorded. The ensemble of these data for various different values of the time delay τ gives the evolution of the system following its excitation by pump pulse [283–287].
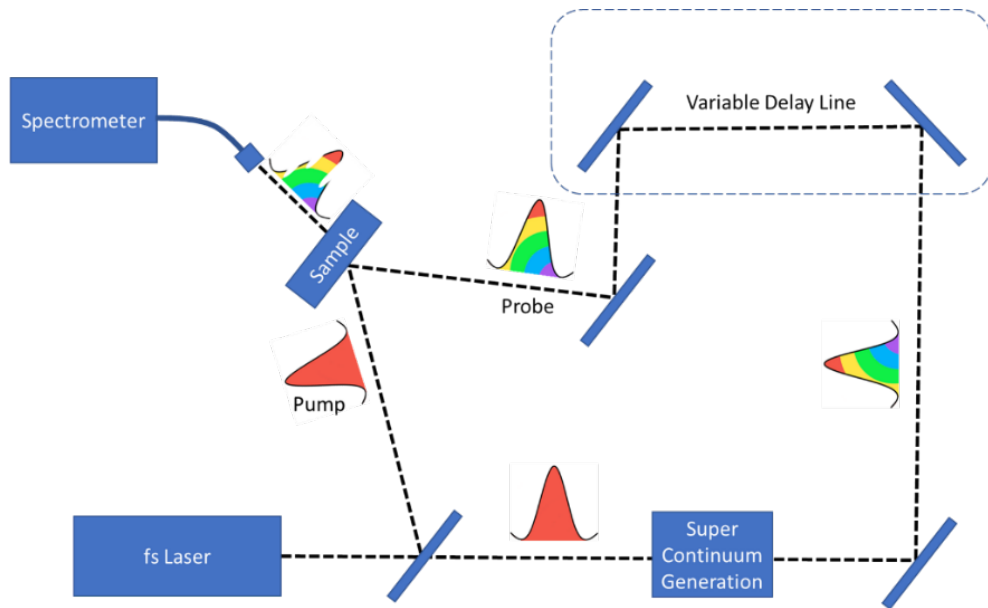

Figure 2.6: Schematic of a transient-absorption spectroscopy setup. Reprinted from Avantes website (https://www.avantes.com/applications/cases/introduction-to-transient-absorption-spectroscopy/).

TAS measurements were performed at the CNR-ISM institute, Division of Ultrafast Processes in Materials (FLASHit), Area della Ricerca di Roma

Tor Vergata. The laser pulses used for exciting and probing the samples were produced by a single femtosecond laser system. This setup consists of a Ti:sapphire oscillator capable of producing $20\,\mathrm{fs}$ pulses with a repetition rate of $80\,\mathrm{MHz}$. A component of the oscillator output is used to seed a chirped pulse amplifier, which produces $4\,\mathrm{mJ}$, $35\,\mathrm{fs}$ pulses centered at $800\,\mathrm{nm}$ with a repetition rate of $1\,\mathrm{kHz}$ [288–290]. An optical parametric amplifier (OPA) is adopted to convert a portion of the amplifier output into tunable light. The OPA output at a wavelength of $1100\,\mathrm{nm}$ is used as the pump pulse. For what concerns the probe, white light supercontinuum (SC) pulses (350–800 nm) are generated by focusing $3\,\mu\mathrm{J}$ of the amplifier radiation into a rotating CaF_2 crystal. The latter is employed in a split-beam configuration in which 50% of the white light passes through the sample while the remaining is used as a reference to take into account pulse-to-pulse fluctuations in the white-light generation. The delay between two following pulses is scanned by varying the optical path of the probing beam. The fact that the measurements was non-invasive was proved by checking the stability of the sample morphology and optical response after the experiment [35, 165, 291].

2.6 Steady-state fluorescence nanothermometry

In order to probe the thermo-induced variation of the PL of the 2D material, an ad-hoc home-assembled setup has been designed and put into use. The main idea of this experimental setup is to focus two distinct laser beams onto the same spot on the sample. One of the beams is meant to locally heat the system by means of the PPT effect, while the second beam is meant to excite the PL from the 2D material used as thermometer. Finally, the PL signal

from the 2D material is collected rejecting all the remaining light by means of suitable filters.

This kind of measurements is particularly challenging for many reasons: first of all the region of interest is very small (of the order of tens of μm), requiring the realization of an integrated optical microscopy functionality; secondly it is necessary to consider that the desired signal (the 2D material PL) is rather weak, and finally that the different wavelengths adopted require different optical components to be manipulated properly.

The working principle and the structure of the steady-state fluorescence nanothermometry setup is schematized in Figure 2.7. Green light with wavelength 532 nm from a laser (a) is adjusted in intensity thanks to a pair of polarizers whose relative orientation can be changed (c). The green light passes through a spatial filter and is focused on the sample by means of a converging lens (e) and a 40× objective (n). A moving shutter is positioned immediately after the laser to enable the collection of the background signal that is not due by the laser-induced PL, but by spurious effects.

White light coming from a broadband source (t) is employed to illuminate the sample for imaging porposes. This light passes through a beam splitter (u) and is then mildly focused on the sample (o) through a 5× objective (p). the light is then collected via the 40× objective (n) and directed to a CMOS camera (g) by means a membrane beam-splitter (f).

The IR light with wavelength 785 nm from a laser diode is directed to the sample by means of two metallic mirrors (r and s) and focused by the 5× objective (p).

The PL signal from the sample is collected by the 40× objective (n) and directed to the spectrometer (m) by means of a beam splitter (h) and a fiber coupler mounted on an optical fiber (l). Before reaching the fiber the light

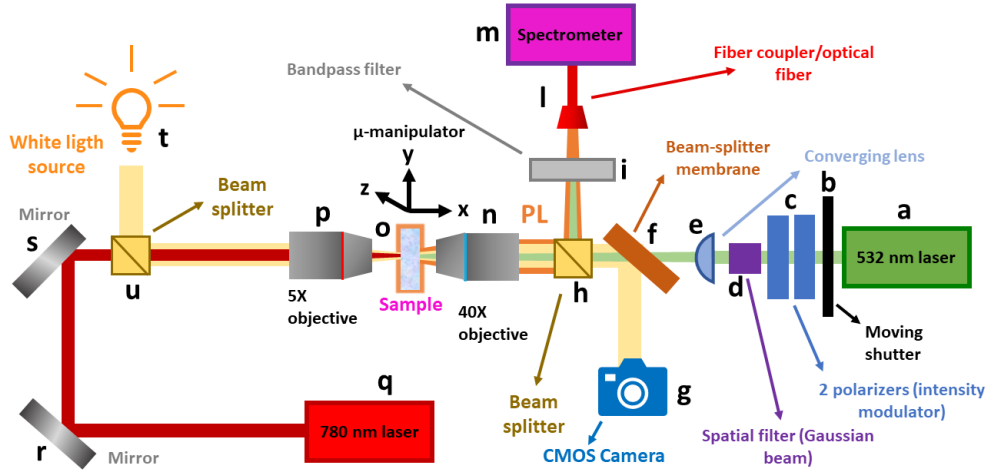beam passes through bandpass filters (i) tuned to the 585-685 nm range. In

Figure 2.7: Schematic of the steady-state fluorescence nanothermometry setup.

order to be sure that the variation of the PL is due only to a thermal effect, spectra are collected when the IR laser is switched off and with the laser on, and the average of the two datsets are finally put in comparison.

2.7 (Imaging) X-ray photoelectron spectroscopy

In order to assess the chemical composition of the sample with spatial nanometric resolution, the samples were analyzed at the ESCA Microscopy beamline at the Elettra Synchrotron Radiation Source in Trieste, by means of a technique called (Imaging) X-ray photoelectron spectroscopy. This technique combines the useful information given by X-ray photoelectron spectroscopy (XPS) with the extreme spatial resolution made possible by the nanometric focusing of the Synchrotron radiation [292, 293].

In the XPS technique electromagnetic radiation in the range of the X-rays is

sent impinging to the sample. The energy of the incoming photons is high enough to extract the electrons from the atoms of the target via the photoelectric effect. By measuring the kinetic energy of the emitted electrons, and knowing the energy of the incident radiation and the workfunction of the material, it is possible to obtain the binding energy of the photoelectrons i.e. the difference in energy between the electronic state and the Fermi energy [294–296]. It is possible in this way to generate an XPS spectrum, where the number of emitted electrons (intensity) is plotted as a function of their binding energy. These graphs contain a chemical information because electrons coming from different atoms engaged in different types of chemical bonds are characterized by their own peculiar binding energy and peak morphology [297–299]. The working principle of XPS is schematized in Figure 2.9.

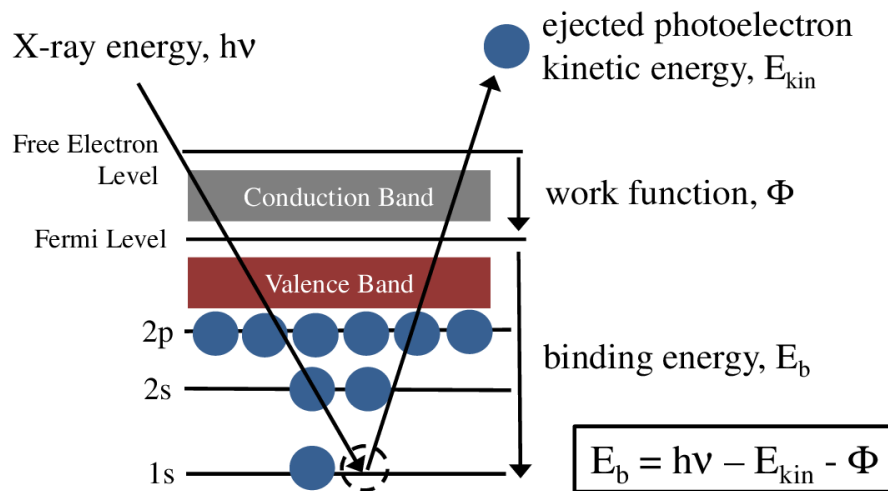With imaging XPS the incident beam is focused down to nanoscopic di-

Figure 2.8: Schematic of the working principle of X-ray photoelectron spectroscopy together with the matematic relationship between the energy of the incident photons, the material workfunction, the kinetic energy of the emitted electrons and the electrons binding energy. Adapted from Ref. [300].

mensions and raster-scanned over the surface of the sample, enabling the

acquisition of super-resolved XPS hypermaps where at each measured point (pixel of the map) is associated an XPS spectra. This is possible only with synchrotron radiation thanks to its unique monochromaticity and brilliance [301, 302].
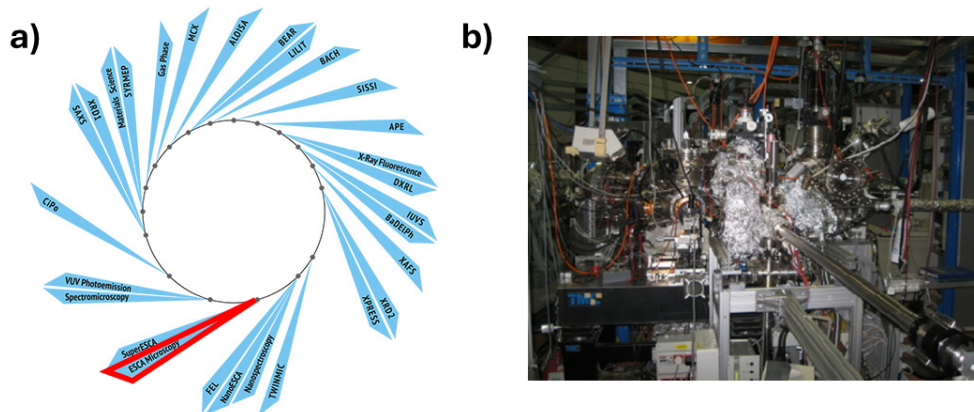

Figure 2.9: a) Sketch of the various beamlines available at Elettra Synchrotron Radiation Source in Trieste where the ESCA Microscopy beamline is highlighted in red. b) Picture of the ESCA Microscopy experimental setup. Panel adapted from the Sissa website (https://www.sissaforschools.it/cosa-si-studia-in-un-sincrotrone/). Panel b reprinted from Central European Research Infrastructure Consortium website (Central European Research Infrastructure Consortium).

Chapter 3

Nanofabrication and characterization of arrays of plasmonic nanostructures

This chapter will focus on the fabrication techniques adopted in order to obtain the plasmonic arrays employed in the nanothermometer devices. The chapter will start with a general introduction to the field of nanolithography and then focus on the patterning techniques and fabrication recipes. The final part of the chapter will present the optical properties of the fabricated plasmonic NP systems.

3.1 Top-down fabrication of nanostructures - general concepts

A nanostructure is broadly defined as an object which has at least on of its spatial dimensions in the 1 nm - 100 nm regime. The increasing demand for

miniaturization of functional components in electronics and optoelectronics together with the interest in studying and exploiting physico-chemical phenomena typical of the nanoscale have been driving an impressive growth of nanofabricated materials, a trend that is not showing any slowdown.

There are two main approaches to obtain nanostructures: it is possible to assemble atoms and molecules until they reach the nanoscale or it is possible to start from spatially extendend objects and to pattern them till obtaining nanostructures. The first one is called *bottom-up* approach, while the second is called *top-down* approach.

Bottom-up methods are generally based on chemical reactions or energy-reduction transformations, they are more suited for large-scale production, but they are not fully deterministic because the results are always determined by the thermodinamic and/or the kinetic of the process.

Top-down approaches (known also as *lithographies*) are usually more expensive and have lower throughput, but they can be completely deterministic: it is possible to choose the geometry and the spatial distribution of the nanostructures with extreme precision.

For the nanothermometer design that we have in mind there are very precise requirements regarding the spectral position and the shape of the LSPR absorption peak of the plasmonic arrays so that also their morphology has to be controlled with great care, for this reason we opted for top-down approaches for the fabrication of the NP.

Among the existing top-down nanolithographic techniques, optical lithograpy is, by far, the most employed in the industry of transistors and microprocessors thanks to its speed and its capability to impress a pattern over a wafer-scale area in a single shot [303–305]. However, its resolution is limited by optical diffraction. The easiest solution to overcome this limit is reduc-

ing the operating wavelength, but this is introducing several technical issues [306]. Moreover, a mask is needed and there's a poor capability of having a three-dimensional (3D) control of the structures [307, 308].

The second most common lithographic technique is the electron-beam lithography (EBL) which is used in the industry for the production of optical lithography masks and in research because of its extreme resolution [309–312]. Despite its grat performances and versatility not all systems can tolerate the high-vacuum conditions or the interaction with energetic particles that are employed in this technique. Indeed, it has been proved that 2D semiconductors can be damaged by the electron beam [313].

This reason, together with the high cost of EBL, is leading to the appearence of other innovative lithographic methods that are gaining a growing interest. Among them Thermal Scanning-Probe Lithography (t-SPL) is emerging as a suitable techique for the patterning and the fabrication on delicate substrates like 2D materials due to its non-invasive thermal-based patterning [314].

With the final goal of obtaining the three-layer nanothermometer described in section 1.4 we adopted both EBL and t-SPL for the fabrication of the plasmonic layers. EBL is best suited for the fabrication of plasmonic NP directly on the transparent substrates because in this way its electron beam cannot cause any damage, and it enables the patterning of wider areas in less time with respect to t-SPL. On the other hand, t-SPL is more appropriate for the fabrication of plasmonic nanostructures direcly on top of 2D materials in a non-invasive and deterministic way. Additionally, t-SPL gives also the possibility to position the NP on the most promising region of the non-homogeneus 2D material [220].

Adopting these two techniques gave us the possibility to obtain many devices and to introduce further degrees of freedom in their fabrication in order to

find the best operating conditions for the nanothermometry measurements. The following sections will be devoted to the description of the two patterning techniques together with their ad-hoc optimized fabrication recipes.

3.2 Electron-beam lithography

3.2.1 Introduction

Electron-beam lithography is considered the most proficient lithographic technique in terms of performances, since a well collimated electron beam can theoretically become the sharpest tool available for nanofabrication, reaching peak resolutions in the order of $2\,nm$ [315]. This is due to the fact that the characteristic wavelenghts of the adopted electrons are much smaller than the wavelengths of lithographic photons so that the electron-beam can be squeezed to nanometric dimension without suffering from diffraction phenomena [316].

The electrons can be generated both by a thermionic source or by a cold cathode [317]. Since electrons are charged particles they can be manipulated by means of electromagnetic fields generated by ad-hoc components called electromagnetic lenses, that change the shape and the behaviour of the beam in order to steer and to focus it on the sample.

It is possible to adopt a standard gaussian beam and create patterns through a raster scan of the beam over the patterning area so that the diameter of the beam is defined as the single pixel of the desired structures, or to adopt a shaped electron beam with the geometry of the desired structures. While the first approach is the most versatile the second one is much faster [318]. A recent progress consists in the use of multiple beams, but despite the promising performances of these new devices they are not common because of their

higher costs [319].

For the fabrication of the structures analized in this thesis a single standard gaussian beam has been adopted.
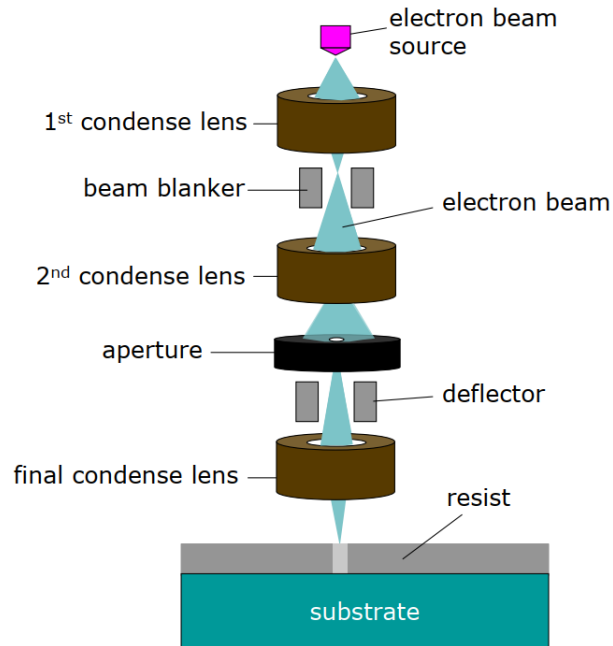

Figure 3.1: Schematic representation of the structure of an electron-beam lithography setup. The electrons are generated via thermo-ionic effect or through cold cathodes and then manipulated by a system of magnetic and electrostatic lenses and focused on the sample. Reprinted from Ref. [320] under a Creative Commons Attribution 4.0 International License (https://creativecommons.org/licenses/by/4.0/).

3.2.2 The fabrication process

The fabrication technique that we adopted is the so called *lift-off*. The heart of this technique is the realization of a pattern (or mask) on an electro-senstitive polymeric material called *electro-resist* that changes its chemical structure after the interaction with the impinging electrons. The electron

bombardment can break the carbon-carbon and hydrogen-carbon bonds creating a rearrangement of the polymeric chains. There are two types of electroresists that behave differently after the interaction with the energetic electrons:

- *positive resists* where the interaction with the electrons causes the breaking of long chains into smaller ones that are more soluble in a suitable mild solvent called *developer*;

- *negative resists* where the interaction with the electrons causes the cross-linking of the chains making them less soluble in the developer on respect to non-crosslinked chains.

For our fabrication we adopted poly(methyl methacrylate), abbreviated as PMMA, that is a positive resist. Its developer is a cold ($4\,°C$) solution of methyl isobutyl ketone (MIBK) in isopropanol (IPA) with a concentration of 1:3 (v/v). In order to guarantee a correct patterning, an electron flux has to be established from the electron source to the sample; since electrons are charged particles, their flux is associated with a current and a current can flow only in a closed electrical circuit. This condition is easily accomplished with conducting or semiconducting substrates, but is not straigthforward for insulating ones.

Since we need optical transparency, we adopted calcium fluoride (CaF_2) substrates that are characterized both by a high optical transmittance, and a high chemical resistance to lithographic processes. However, CaF_2 is an electrical insulator so that it is impossible to adopt this material as a substrate for electron-beam patterning as it is.

We solved this problem by coating the PMMA resist deposited on top of CaF_2 with $10\,nm$ of alluminum (Al) via thermal evaporation. The surface

of the sample is then electrically connected with the metallic sample holder with a special metallic clip. The fabrication process (schematized in Figure 3.2) is organized through the following steps:

- the CaF_2 substrate is cleaned and its surfaces is made more hydrofilic (activation) through oxygen plasma treatment (180 s, 100 W and 100 % of oxygen);

- PMMA in concentration A2 (80% w/w) is deposited on substrates via spin coating (1800 rpm for 60 s);

- the resist is subject to a baking treatment (180 °C for 7 min);

- the sample is coated with 10 nm of Al via thermal evaporation;

- EBL patterning is performed with the instrument RAITH ® 150-2;

- Al removal is performed by a one molar (1M) aqueous solution of potassium hydroxide (KOH) for 20 s;

- the sample is cleaned in deionized water (DIW);

- the pattern is developed in MIBK in IPA 1/3 (v/v);

- the development is stopped by rising the sample in IPA for 30 s;

- the metal deposition is performed via electron-beam evaporation;

- the resist is removed in agitated acetone (lift-off process).

In order to guarantee a correct mask-effect from the developed resist the creation of the so-called *undercut* is necessary. The undercut consists in the presence of a cavity under the patterned region which is slightly larger than the patterned structures as it is shown in Figure 3.2. For EBL the creation of

the undercut cavity is guaranteed by the particular electron-matter interaction that creates a volume of interaction with the characteristic "pear" shape due to the presence of scattered and secondary electrons.

Another crucial issue for the reliability of the process is the choice of the
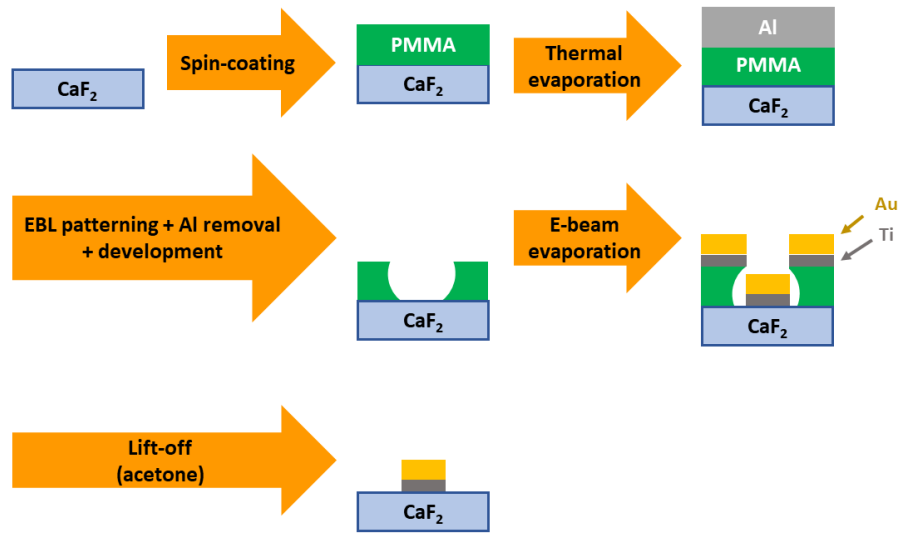

Figure 3.2: Schematic of the main steps of the fabrication process with EBL patterning followed by lift-off for the realization of arrays of plasmonic NP.

correct metal thickness to be deposited on the patterned resist. In our case two metals have to be deposited: titanium (Ti) and (Au). The first one is necassary because it behaves as an adhesion layer avoiding the detachment of gold from the substrate caused by the high interfacial energy between Au and CaF_2. We found that $5\,\text{nm}$ of Ti and $35\,\text{nm}$ of Au are fine for a repeatable outcome and for good plasmonic properties. The general rule of thumb is that the metal thickness has to be less than $2/3$ of the resist thickness (in our case around $100\,\text{nm}$) in order to let the lift-off process take place in the correct way.

3.2.3 Tuning of the plasmonic optical response

As described in the subsection 1.2.2 the optical response of arrays of plasmonic NPs is greatly affected by the size, the shape and the spatial arrangements of the nanostructures. Our final goal is the optimization of the spectral position and shape of the plasmonic layer to make it a suitable nano-heater to be coupled with the WS_2 nano-thermometer layer (section 1.4). To do this, many geometries, characterized by different shapes and spatial distribution of the NP, were tested.

Another crucial parameter for the fabrication of nanostructures via EBL is the electron dose employed to perform the patterning, i.e. the amount of electrons per unit area in the exposed regions. Keeping fixed the nominal geometry and increasing the electron dose, the effect is the expansion of the lateral size of the structures with a consequent shrinking of the interparticle distance in case of neighbouring structures. The consequence of these two combined effects is the progressive redshift of the LSPR of the obtained arrays with an increase of the adopted electron dose.

For the purpose of the present thesis, three families of geometries were adopted:

- circular (nanodisks) denoted as "C",

- rectangular (nanorods) with smaller aspect-ratio denoted as "L1",

- rectangular (nanorods) with higher aspect-ratio denoted as "L2".

For each family the dimensions were changed in order to obtain three geometries for each family:

- nanodisks with nominal diameter of 50 nm denoted as "C50",

- nanodisks with nominal diameter of 75 nm denoted as "C75",

- nanodisks with nominal diameter of 90 nm denoted as "C90",

- nanorods with nominal dimensions 50 nm×100 nm denoted as "L1-50",

- nanorods with nominal dimensions 75 nm×125 nm denoted as "L1-75",

- nanorods with nominal dimensions 90 nm×140 nm denoted as "L1-90",

- nanorods with nominal dimensions 50 nm×150 nm denoted as "L2-50",

- nanorods with nominal dimensions 75 nm×175 nm denoted as "L2-75",

- nanorods with nominal dimensions 90 nm×190 nm denoted as "L2-90".

For all these geometries the nominal gap between neighbouring structures was kept fixed at 100 nm. Figure 3.3 a) reports a sketch which summarizes all the adopted geometries.

The unit cell of all the geometries was repeated in order to cover an area of $30 \times 30 \, \mu\text{m}^2$ and each one of the squares obtained was repeated four times changing the electron dose factor from 4 to 7 by step of 1. The dose factor indicates the number of times the fundamental dose ($100 \, \mu\text{C/cm}^2$) is employed, for example a dose factor 5 means that the effective dose is $5 \times (100 \, \mu\text{C/cm}^2)$ $= 500 \, \mu\text{C/cm}^2$. We did not use dose values smaller than $400 \, \mu\text{C/cm}^2$ because we proved that they were insufficient to enable the fabrication.

The dimensions of the patterned regions for these tests need to be wide enough to perform micro-transmission spectroscopy of each area, but small enough to obtain acceptable EBL patterning times. We found that $30 \times 30 \, \mu\text{m}^2$ is a good compromise. All the patterned areas are summarized in Figure 3.3 b).
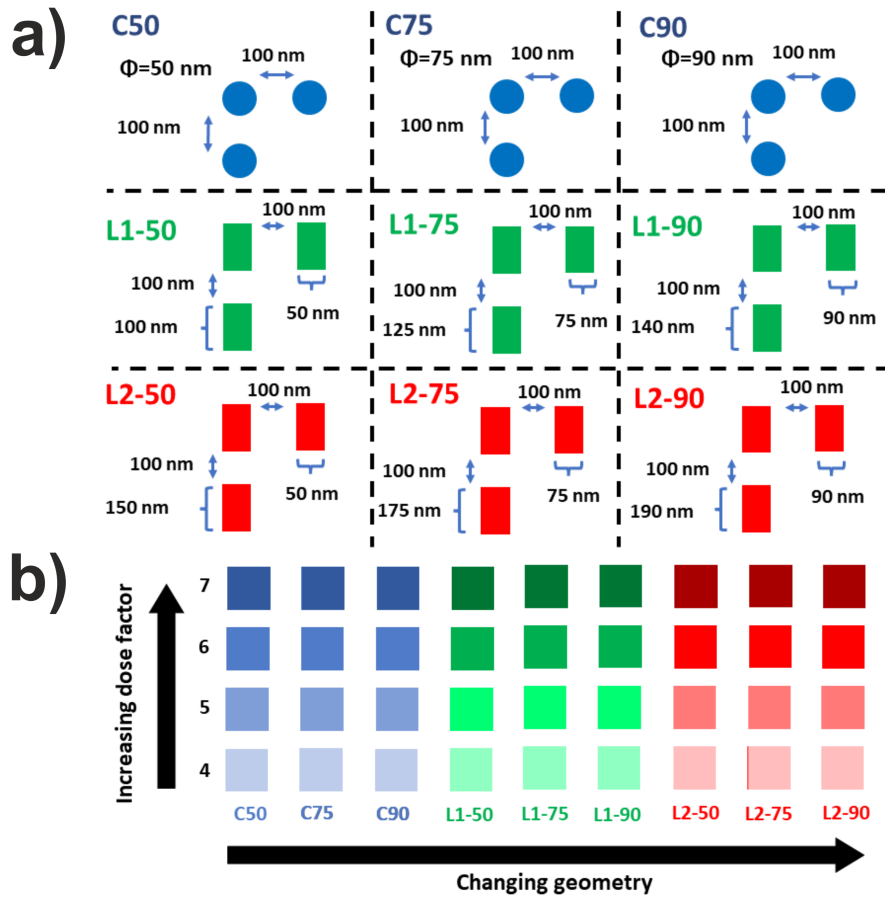
Figure 3.3: a) Scheme of all the nominal geometries. b) Scheme of all the patterned areas with different geometries and dose factors. Each area is $30 \times 30 \, \mu m^2$ wide.

3.2.4 Plasmonic arrays characterization

All the patterned areas were characterized morphologically by means of Scanning Electron Microscope (SEM) (Helios ® NanoLab 650) and optically by means of micro-transmittance spectroscopy with two orthogonal polarization states of the probing light. With these rich matrices of arrays with different geometries and dose factors and through the employment of polarized light it is possible to obtain a fine tuning of the optical response of the arrays of plasmonic nanoparticles over a broad spectral range.

85

Figure 3.4 reports the results of the characterization of the arrays of the "C" family. Figure 3.4 a), b) and c) reports the relative transmission spectra of
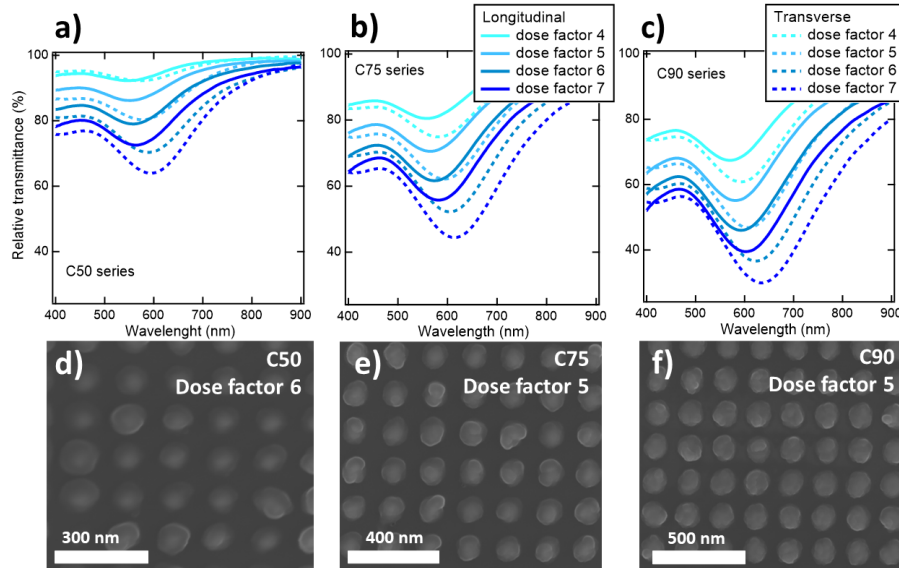

Figure 3.4: Relative transmittance spectra (obtained with two orthogonal polarization states of the probing light) of the arrays fabricated with different dose factors of the "C" family: a) C50 group, b) C75 group and c) C90 group. SEM micrographs of some arrays of the "C" family: d) C50 dose factor 6, e) C75 dose factor 5, f) C90 dose factor 5 (accelerating voltage 20 kV).

the arrays of the group C50, C75 and C90 respectively obtained with different dose factors and with two configuration of the polarization state of the impinging light.

The two orthogonal polarization states of the probing light are noted as "longitudinal" and "trasverse". The C family is the one were nanostructures are nominally nanodisks, but probing with these two polarization states enables the estimation of the anisotropy of the fabricated structures. The notation of "longitudinal" and "trasverse" is only kept for coherence wiht the following characterization of the "L1" and "L2" families wich are made of anisotropic structures (nanorods).

The spectra corresponding to the different doses are indicated with different shades of blue moving from the lighter to the darker increasing the dose factor; longitudinal and transverse measures are noted with continuous and dashed lines respectively. From the relative transmission spectra it is possible to notice the presence of a single transmission dip which is due to the excitation of the dipolar mode of the LSPR. It is possible to follow the transformation of the system with the increase of the adopted dose: increasing the dose the nanostructures get bigger and the gap between them is consequently reduced. As explained in the subsection 1.2.2 this causes a reduction of the transmittance (due to an increase of the effective metal coverage) and a redshift of the absorption peak (due to to an increase of the interparticle interaction). Moving from the graphs a) to b) to c) it is possible to follow the evolution of the optical response of the system after a change in the diameter of the nanodisks, without changing the gap: the LSPR peak is redshifted (from resonance wavelengths $\lambda_{LSPR} \simeq 540$ nm to 660 nm) as a function of increasing diameter and the overall transmission is reduced (due to an increase of the metal coverage). A discrepancy between longitudinal and transverse measures can be spotted and this indicates a deviation from the nominal circular shape.

For the sake of simplicity only three SEM micrographs are reported: Figure 3.4 d) C50 dose factor 6, e) C75 dose factor 5 and f) C90 dose factor 5 (accelerating voltage $20\,\text{kV}$). From this images it is possible to indentify the nanostructures and to extimate their morphology. In particular, we observe that they are more elongated in the horizontal direction (here probed in the "trasverse" configuration) and this explains the difference between "longitudinal" and "trasverse" transmission spectra. It is possible to spot also "bubble-like" structures on the NPs, corresponding to crystalline grains of

the deposited metal.

Figure 3.5 reports the results of the characterization of the arrays of the "L1" family. Figure 3.5 a), b) and c) report the relative transmission spectra of
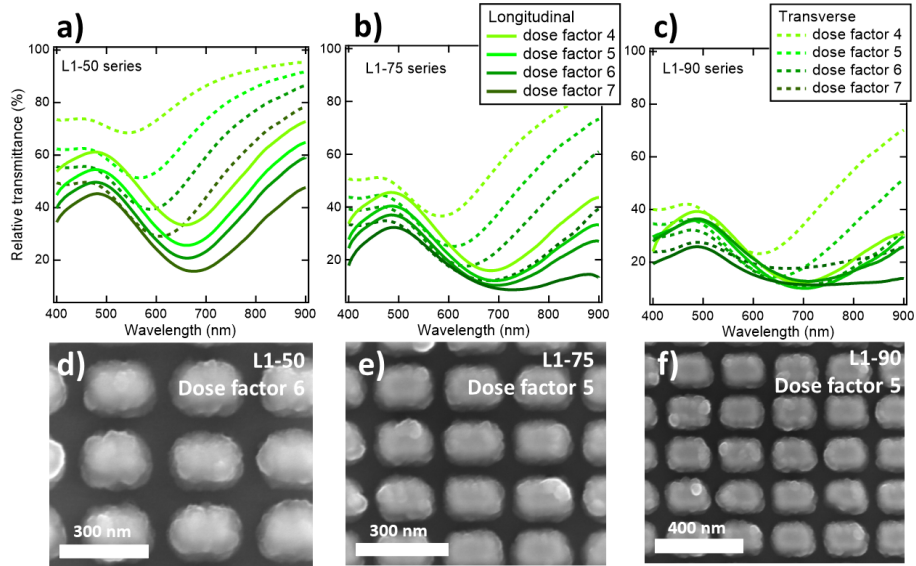

Figure 3.5: Relative transmittance spectra obtained with light polarization parallel to the long (longitudinal) and short (transverse) axis of the structures of the different arrays and dose factors of the "L1" family: a) L1-50 group, b) L1-75 group and c) L1-90 group. SEM micrographs of some arrays of the "L1" family: d) L1-50 dose factor 6, e) L1-75 dose factor 5, f) L2-90 dose factor 5 (accelerating voltage 20 kV).

the arrays of the group L1-50, L1-75 and L1-90 respectively obtained with different dose factors and with two configuration of the polarization state of the impinging light: parallel to the longer (longitudinal) and to the shorter (transverse) axis of the nanorods.

The spectra of the different doses are indicated with different shades of green moving from the lighter to the darker upon increasing the dose factor, longitudinal and transverse measures are noted with continuous and dashed lines respectively. From the relative transmission spectra 3.5 a), b) and c) it is possible to notice the presence of a single transmission dip which is due to